

# Quantum Circuits: Divide and Compute with Maximum Likelihood Tomography

Michael A. Perlin,<sup>1,2</sup> Zain H. Saleem,<sup>3</sup> Martin Suchara,<sup>3</sup> and James C. Osborn<sup>2,4</sup>

<sup>1</sup>*JILA, National Institute of Standards and Technology and University of Colorado, 440 UCB, Boulder, Colorado 80309, USA*

<sup>2</sup>*Argonne Leadership Computing Facility, Argonne National Laboratory, 9700 S. Cass Avenue, Lemont, Illinois 60439*

<sup>3</sup>*Mathematics and Computer Science Division, Argonne National Laboratory, 9700 S. Cass Avenue, Lemont, Illinois 60439*

<sup>4</sup>*Computational Science Division, Argonne National Laboratory, 9700 S. Cass Avenue, Lemont, Illinois 60439*

(Dated: 2021-10-04)

We introduce maximum likelihood fragment tomography (MLFT) as an improved circuit cutting technique for running “clustered” quantum circuits on quantum devices with a limited number of qubits. In addition to minimizing the classical computing overhead of circuit cutting methods, MLFT finds the most likely probability distribution for the output of a quantum circuit, given the measurement data obtained from the circuit’s fragments. Unlike previous circuit cutting methods, MLFT guarantees that all reconstructed probability distributions are strictly non-negative and normalized. We demonstrate the benefits of MLFT for accurately estimating the output of a fragmented quantum circuit with numerical experiments on random unitary circuits. Finally, we provide numerical evidence and theoretical arguments that circuit cutting can estimate the output of a clustered circuit with higher fidelity than full circuit execution, thereby motivating the use of circuit cutting as a standard tool for running clustered circuits on quantum hardware.

## I. INTRODUCTION

The advent of noisy intermediate-scale quantum (NISQ) technologies [1] makes quantum processors with increasing numbers of qubits available to the quantum computing community for experimentation. The rapid progress in the development and manufacturing of these devices is remarkable, with state-of-the-art superconducting quantum processors reaching  $\sim 50$  qubits with percent-level gate and readout errors [2–4]. Advances on the hardware front have been matched by the theoretical development of suitable hardware benchmarks [5], which have in turn enabled proof-of-principle demonstrations of a computational advantage over classical computing systems [4].

Despite tremendous progress, existing devices still lack the number and quality of qubits required for practical NISQ-era applications such as digital quantum simulation [6, 7], quantum optimization [8–10] and quantum machine learning [11, 12]. Without error correction, these applications are severely limited by the accumulation of errors that will only compound as devices scale up to more qubits and deeper circuits. Bridging the gap between the requirements of NISQ-era quantum algorithms and the capabilities of NISQ devices will require error mitigation techniques [13, 14] and problem decompositions that trade quantum and classical computing resources [15, 16].

One decomposition, inspired by the fragmentation methods used for quantum molecular cluster simulations [17–19], applies fragmentation to the execution of quantum circuits [16]. This decomposition consists of first “cutting” a quantum circuit into smaller subcircuits, or *fragments*, that can be executed on processors with fewer qubits, and then reconstructing the probability distribution over measurement outcomes for the original quantum circuit from probability distributions associated with its fragments. The severed quantum connections between

circuit fragments are essentially simulated by classical post-processing of fragment data, which leads to a classical computing overhead that grows exponentially with the number of cuts that are made to a circuit. This approach is therefore suitable for simulating circuits that are decomposable into clusters of gates with a small number of inter-cluster interactions. Such circuits make appearances in near-term quantum computing applications such as the quantum approximate optimization algorithm (QAOA) [8, 9] and variational quantum eigensolvers (VQE) [16, 20].

Due to the presence of fundamental shot noise (in essence, finite sampling error), an unavoidable feature of the original fragment recombination method in Ref. [16] is that the distribution over measurement outcomes obtained by characterizing and recombining circuit fragments does not generally satisfy central axioms of probability theory, namely that a probability distribution must be non-negative and normalized. A naive fix to this problem would be to simply remove all negative probabilities and normalize the reconstructed distribution in question. In the spirit of maximum likelihood state tomography (MLST) [21], however, one would like to determine the “most likely” probability distribution that is consistent with available fragment data.

In this work, we find this “most likely” probability distribution by generalizing MLST and introducing maximum likelihood fragment tomography (MLFT), the use of which guarantees that reconstructed probability distributions are non-negative and normalized. We discuss how MLFT minimizes the classical computing resources necessary to characterize circuit fragments, and introduce a tensor-network-based fragment recombination method that allows for the use of efficient numerical routines. We test our methods in numerical experiments with random unitary circuits, and demonstrate that MLFT estimates the probability distribution at the output of a fragmented quantum circuit with higher fi-

delity than the naive method of removing negative probabilities and normalizing. As an added bonus, we find that circuit cutting methods can outperform direct execution and sampling of a clustered circuit for the task of estimating a circuit's associated probability distribution with a fixed number of queries to quantum hardware (known as “shots” or “trials” in e.g. Qiskit [22] or pyQuil [23]). We provide theoretical arguments to support this finding, which motivates the use of circuit cutting as a standard tool for evaluating clustered circuits on quantum hardware, even when all hardware requirements for full circuit execution are satisfied.

In Section II we provide an overview of the circuit cutting method introduced in Ref. [16], before discussing the shortcomings of this method in Section III. We then introduce the procedure of MLFT in Section IV, in addition to the tensor-network-based fragment recombination method that it enables. To test out our ideas and demonstrate their utility in an application-agnostic setting, we perform numerical experiments on clustered random unitary circuits in Section V, and we discuss our main conclusions and future outlooks in Section VI.

## II. THE GENERAL CUT-AND-STITCH PRESCRIPTION

Here we provide a basic overview of the circuit cutting procedure introduced in Ref. [16], and establish terminology that we will use throughout the remainder of this work. Given an arbitrary quantum state  $|\psi\rangle$  of  $N$  qubits, a straightforward resolution of the identity operator  $I = \sum_{b \in \{0,1\}} |b\rangle\langle b|$  on qubit  $n$  implies that

$$|\psi\rangle = I_n |\psi\rangle \simeq \sum_{b \in \{0,1\}} |b\rangle \otimes {}_n\langle b| \psi\rangle, \quad (1)$$

where  $I_n$  denotes the action of  $I$  on qubit  $n$ ; the relation  $\simeq$  denotes equality up to a permutation of tensor factors (i.e. qubit order); and  ${}_n\langle b| \psi\rangle$  is a sub-normalized state of  $N - 1$  qubits acquired by projecting  $|\psi\rangle$  onto state  $|b\rangle$  of qubit  $n$ . If the structure of a quantum circuit that prepares  $|\psi\rangle$  allows, a similar resolution of the identity operator  $I$  can be used to “cut” the circuit by inserting  $I$  at a location that splits the circuit into two disjoint sub-circuits. For example, if  $|\psi\rangle = V_{23}U_{12}|000\rangle$ , where  $U_{12}$  and  $V_{23}$  are the two-qubit gates  $U$  and  $V$  acting on qubits 1, 2 and 2, 3, then by inserting the identity operator  $I_2$  (on qubit 2) between  $U_{12}$  and  $V_{23}$  we find that

$$|\psi\rangle \simeq \sum_{b \in \{0,1\}} |\psi_1(b)\rangle \otimes |\psi_2(b)\rangle, \quad (2)$$

where the factors

$$|\psi_1(b)\rangle \equiv {}_2\langle b| U |00\rangle, \quad |\psi_2(b)\rangle \equiv V |b0\rangle \quad (3)$$

are (generally sub-normalized) “conditional” states prepared by projecting onto  $|b\rangle$  or preparing  $|b\rangle$ , as appropriate. The identity in Eq. (2) is visualized in Figure 1,

albeit with the use of density operators that we discuss below.

The above splitting method relies on the capability to project qubit  $n$  onto state  $|b\rangle$  while preserving phase information. Such capability is possible when running classical simulations of a circuit, but is not possible on quantum computing hardware. This limitation can be overcome by representing quantum states  $|\psi\rangle$  with density operators  $\rho = |\psi\rangle\langle\psi|$ , whose diagonal entries in a given measurement basis define a classical probability distribution over measurement outcomes in that basis. For ease of language, we will at times blur the distinction between a state  $\rho$  and the probability distribution defined by its diagonal entries in a fixed computational basis. In the remainder of this work, we will discuss circuit splitting and reconstruction in way that is compatible with circuit execution on quantum computing hardware. Nonetheless, our methods can be applied just as well to classical state simulation, with minor simplifying modifications to account for the added capability of performing deterministic, phase-preserving qubit projections.

The identity analogous to Eq. (1) for density operators  $\rho$  reads

$$\rho \simeq \frac{1}{2} \sum_{M \in \mathcal{B}} M \otimes \text{tr}_n(M_n \rho), \quad (4)$$

where  $\mathcal{B}$  is a basis of self-adjoint  $2 \times 2$  matrices with normalization  $\text{tr}[M^{(i)}M^{(j)}] = 2\delta_{ij}$  for  $M^{(i)}, M^{(j)} \in \mathcal{B}$ ;  $\text{tr}_n$  denotes a partial trace with respect to qubit  $n$ ; and  $M_n$  with  $n \in \mathbb{Z}_n$  denotes an operator that acts with  $M$  on qubit  $n$  and trivially (i.e. with the identity  $I$ ) on all other qubits. To be concrete, we will use the set of Pauli operators together with the single-qubit identity operator,  $\mathcal{B} \equiv \{X, Y, Z, I\}$ , as our basis. The identity in Eq. (4) implies that the state prepared by the action of a three-qubit circuit  $V_{23}U_{12}$  on the trivial state  $|0\rangle\langle 0|^{(3)}$  can be decomposed as

$$\rho \simeq \frac{1}{2} \sum_{M \in \mathcal{B}} \rho_1(M) \otimes \rho_2(M), \quad (5)$$

where now the factors

$$\rho_1(M) \equiv \text{tr}_2\left(M_2 U |0\rangle\langle 0|^{(2)} U^\dagger\right), \quad (6)$$

$$\rho_2(M) \equiv V(M \otimes |0\rangle\langle 0|) V^\dagger, \quad (7)$$

have no straightforward interpretation as “conditional” states, as with  $|\psi_1(b)\rangle$  and  $|\psi_2(b)\rangle$  in Eq. (2). In order to decompose  $\rho$  into conditional states, the idea in Ref. [16] was essentially to expand each  $M \in \mathcal{B}$  into its eigenbasis:

$$\rho \simeq \frac{1}{2} \sum_{M \in \mathcal{B}} \sum_{r,s \in \lambda(M)} r s \rho_1(M_r) \otimes \rho_2(M_s), \quad (8)$$

where  $\lambda(M)$  denotes the spectrum of  $M$ , i.e.  $\lambda(X) = \lambda(Y) = \lambda(Z) = (+1, -1)$  and  $\lambda(I) = (1, 1)$ ; and  $M_s \equiv |M_s\rangle\langle M_s|$  with  $s \in \lambda(M)$  is a projector onto an eigenstate

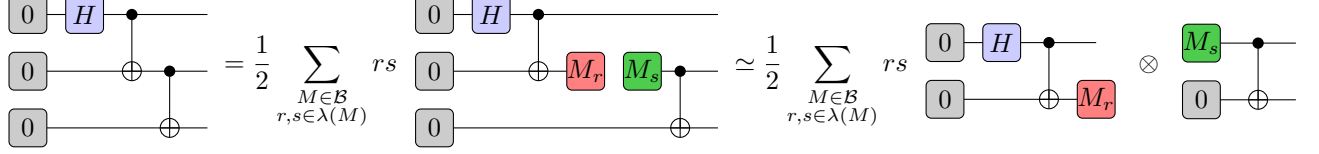


FIG. 1. A 3-qubit GHZ circuit cut into two 2-qubit fragments by inserting an identity operator. Here  $\mathcal{B} \equiv \{X, Y, Z, I\}$  is the set of Pauli operators  $X, Y, Z$  and the identity  $I$ , which together form an orthogonal basis for the space of single-qubit operators;  $\lambda(M)$  denotes the spectrum of  $M$ ; and  $M_s \equiv |M_s\rangle\langle M_s|$  is the projector onto an eigenstate  $|M_s\rangle$  of  $M$  with eigenvalue  $s$ . Green (red) boxes labeled by the state  $M_s$  ( $M_r$ ) correspond to preparations (projections) of a qubit in the corresponding state. After cutting a circuit, the resulting fragments can be simulated independently, and an appropriate post-processing of simulation results recovers the output of the original (pre-cut) circuit.

of  $|M_s\rangle$  of  $M$  with eigenvalue  $s$ . Note that the choice of eigenstates for the identity operator  $I$  is arbitrary as long as these two states are orthogonal, so we can reuse the eigenstates from one of the other operators.

The decomposition in Eq. (8) allows interpreting each  $\rho_f(M_s)$  as a conditional state, obtained either by post-selecting onto the measurement of a qubit in state  $|M_s\rangle$ , or by preparing a qubit in state  $|M_s\rangle$ , as appropriate (see Figure 1). The decomposition in Eq. (8) thus corresponds to the following procedure for circuit cutting and reconstruction: after cutting a circuit into (say) two fragments, characterize the classical probability distributions  $\rho_f(M_s)$  over measurement outcomes by running the corresponding sub-circuit and either post-selecting on measurement outcomes  $M_s$  or preparing states  $M_s$ , as appropriate. Note that post-selected probability distributions are generally sub-normalized, and the normalization  $\text{tr } \rho_1(M_s)$  is equal to the probability of getting outcome  $M_s$  when measuring in the diagonal basis of  $M$ . After characterizing the conditional distributions  $\rho_f(M_s)$  for each of  $f \in \{1, 2\}$ ,  $M \in \{X, Y, Z\}$ , and  $s \in \{+1, -1\}$ , combine these distributions according to Eq. (8). This scenario is illustrated in Figure 1, which cuts a 3-qubit GHZ circuit preparing the state  $|\psi\rangle \propto |000\rangle + |111\rangle$  into two 2-qubit fragments.

### III. SHORTCOMINGS OF PREVIOUS WORK

In practice, recombining circuit fragments as prescribed by Eq. (8) is inefficient in two ways. First, the tensor products in Eq. (8) are a computational bottleneck for fragment recombination. It is therefore faster to post-process conditional distributions by first (i) for each fragment  $f$ , combining the six independent distributions  $\rho_f(M_s)$  into four distributions:  $\rho_f(M) = \rho_f(M_{+1}) - \rho_f(M_{-1})$  for each  $M \in \{X, Y, Z\}$  and  $\rho_f(I) = \rho_f(M_{+1}) + \rho_f(M_{-1})$  for any  $M \in \{X, Y, Z\}$ , and then (ii) combining the fragment distributions  $\rho_f(M)$  according to Eq. (5). In a circuit with  $K$  cuts, this post-processing reduces the number of tensor products that must be computed during recombination from  $16^K$  to  $4^K$ , which is an exponential improvement in

$K^a$ .

Second, the recombination formula in Eq. (8) nominally requires, for each fragment  $f$  incident on  $K_f$  cuts, characterizing  $K_f^6$  probability distributions. This characterization is overcomplete, because the  $K_f^6$  distributions are not all linearly independent. In the case of a fragment with a single incident cut, for example, we can decompose

$$\rho_f(X_-) = \rho_f(Z_+) + \rho_f(Z_-) - \rho_f(X_+). \quad (9)$$

In fact, a fragment with  $K_f$  incident cuts can be completely characterized by  $K_f^4$  distributions, which can be deduced from the fact that the space of operators on the Hilbert space of a qubit has real dimension four. The symmetric, informationally complete, positive operator-valued measure (SIC-POVM)  $\{\Pi_j^{\text{SIC}} : j \in \mathbb{Z}_4\}$  (consisting of projectors  $\Pi_j^{\text{SIC}}$  onto the states represented by the four corners of a regular tetrahedron inscribed in a Bloch sphere), for example, form a mutually unbiased basis for the space of single-qubit operators. Given any single-qubit operator  $M$ , we can therefore expand  $\rho_f(M) = \sum_{j \in \mathbb{Z}_4} c_{Mj}^{(f)} \rho_f(\Pi_j^{\text{SIC}})$  with real coefficients  $c_{Mj}^{(f)}$ .

Finally, characterizing fragments is a noisy process, due to both (i) hardware errors that are unavoidable without error correction, as in all NISQ devices, and (ii) statistical sampling (shot) noise. As a result, the “experimentally inferred” distributions  $\tilde{\rho}_f(M_s)$  approximating the “true” distributions  $\rho_f(M_s)$  will generally contain errors, and will fail to satisfy self-consistency conditions such as Eq. (9). As a consequence, when combining these distributions according to Eqs. (5) and (8) there is similarly no guarantee that the reconstructed probability distribution will satisfy conditions required of a probability distribution, such as non-negativity and normalization.

To fix these shortcomings, in the following section we recast the task of characterizing conditional distributions

<sup>a</sup> The recombination procedure in Ref. [16] involves  $8^K$  terms, rather than  $16^K$ , because it essentially post-processes “measurement” conditions, but not “preparation” conditions, collapsing the sum over  $r$  in Eq. (8) but leaving the sum over  $s$ .

into the task of performing fragment tomography, treating the fragments  $\rho_f$ , rather than distributions  $\rho_f(M_s)$ , as first-class objects. In addition to being automatically efficient in terms of the classical memory footprint of characterizing each fragment, performing fragment tomography allows us to adapt the method of maximum likelihood tomography [21] to construct a model for each fragment that is, by construction, guaranteed to satisfy all appropriate self-consistency conditions. Fragment recombination is then similarly guaranteed to yield a probability distribution that is both non-negative and normalized. Finally, we show how the fragment models constructed via fragment tomography naturally admit a tensor-network-based method for recombination, which allows for the use of efficient numerical routines that outperform the recombination procedures discussed so far.

#### IV. MAXIMUM LIKELIHOOD FRAGMENT TOMOGRAPHY

Once a circuit has been cut into fragments  $\rho_f$ , rather than characterizing conditional distributions  $\rho_f(M_s)$  we can perform a more systematic *maximum likelihood fragment tomography* (MLFT) procedure to characterize these fragments. The purpose of MLFT is to perform a “maximum likelihood” characterization, similar to the characterization of quantum states in Ref. [21], which guarantees that any probability distribution associated with these fragments will be (i) the “most likely” distribution consistent with available fragment data, while (ii) satisfying all necessary constraints for a valid (i.e. non-negative and normalized) probability distribution. MLFT is essentially a type of quantum process tomography, which generalizes maximum likelihood state tomography (MLST) [21] to the case of channels (processes) with mixed (quantum/classical) inputs and outputs.

Any given fragment, nominally a unitary circuit on  $Q$  qubits, will generally have  $Q_i$  “quantum input” and  $Q_o$  “quantum output” qubits at the locations of cuts. We refer to these inputs and outputs as “quantum” because characterizing the fragment for circuit reconstruction will require performing full quantum tomography on the corresponding degrees of freedom. In contrast, the remaining  $C_i \equiv Q - Q_i$  “classical input” qubits are always initialized in the trivial state  $|0\rangle_i \equiv |0\rangle^{\otimes C_i}$ , and the remaining  $C_o \equiv Q - Q_o$  “classical output” qubits are always measured in a fixed computational basis. For definiteness, we can first think of a fragment as a quantum channel  $\mathcal{E}_\Lambda$  on the state of  $Q$  qubits. The channel-state duality [24–26] implies that this channel is uniquely defined by a 4-partite state (density operator)  $\Lambda$  defined by

$$\Lambda \equiv \sum_{\substack{k,\ell,m,n \\ p,q,r,s}} \Lambda_{k\ell;mn;pq;rs} |k\rangle\langle\ell| \otimes |m\rangle\langle n| \otimes |p\rangle\langle q| \otimes |r\rangle\langle s|, \quad (10)$$

where the bitstrings  $k, \ell (m, n; p, q; r, s)$  index states in the Hilbert space of the quantum input (classical input; quantum output; classical output) qubits of the fragment, and are implicitly summed over  $\mathbb{Z}_2^{Q_i}$  ( $\mathbb{Z}_2^{C_i}$ ;  $\mathbb{Z}_2^{Q_o}$ ;  $\mathbb{Z}_2^{C_o}$ ). Specifically, the channel  $\mathcal{E}_\Lambda$  maps a bipartite input state

$$\rho \otimes |\mathbf{0}_i\rangle\langle\mathbf{0}_i| \equiv \sum_{k,\ell} \rho_{k\ell} |k\rangle\langle\ell| \otimes |\mathbf{0}_i\rangle\langle\mathbf{0}_i| \quad (11)$$

at its input to the bipartite state

$$\mathcal{E}_\Lambda(\rho \otimes |\mathbf{0}_i\rangle\langle\mathbf{0}_i|) \equiv \sum_{k,\ell,p,q,r,s} \Lambda_{k\ell;0,0;pq;rs} \rho_{k\ell} |p\rangle\langle q| \otimes |r\rangle\langle s| \quad (12)$$

at its output. To account for the fact that classical outputs are only ever measured in a fixed computational basis, we can remove all parts of  $\mathcal{E}_\Lambda(\rho)$  that are off-diagonal with respect to the measurement basis of the corresponding qubits. In total, we therefore need only characterize the channel  $\tilde{\mathcal{E}}_\Lambda$  defined by

$$\mathcal{E}_{\tilde{\Lambda}}(\rho) \equiv \sum_{k,\ell,p,q,s} \tilde{\Lambda}_{k\ell;pq;s} \rho_{k\ell} |p\rangle\langle q| \otimes |s\rangle\langle s|, \quad (13)$$

where

$$\tilde{\Lambda}_{k\ell;pq;s} \equiv \Lambda_{k\ell;0,0;pq;ss}. \quad (14)$$

The task of performing MLFT thus reduces, in essence, to performing tomography on the tri-partite block-diagonal state

$$\tilde{\Lambda} \equiv \sum_{k,\ell,p,q,s} \tilde{\Lambda}_{k\ell;pq;s} |k\rangle\langle\ell| \otimes |p\rangle\langle q| \otimes |s\rangle\langle s| \quad (15)$$

$$= \sum_s \tilde{\Lambda}_s \otimes |s\rangle\langle s|, \quad (16)$$

where Eq. (16) implicitly defines the blocks  $\tilde{\Lambda}_s$ . In words, the reduced state  $\tilde{\Lambda}$  is acquired from the full state  $\Lambda$  by conditioning on (i.e. fixing) a trivial state  $|\mathbf{0}_i\rangle\langle\mathbf{0}_i|$  on its classical inputs, and the block  $\tilde{\Lambda}_s$  is acquired from  $\tilde{\Lambda}$  by conditioning on measurement of the bitstring  $s$  on its classical outputs. The relationship between  $\Lambda$ ,  $\tilde{\Lambda}$ , and  $\tilde{\Lambda}_s$  is sketched out in Figure 2.

In a nutshell, MLFT is performed by providing a variety of quantum inputs to  $\tilde{\Lambda}$ , and measuring its quantum outputs in a variety of bases. The blocks  $\tilde{\Lambda}_s$  are inferred by least-squares fitting to a linear operator that maps quantum inputs to quantum outputs, using all available data from experiments in which bitstring  $s$  was observed on the classical outputs of a fragment. This procedure yields an experimental ansatz state  $\Lambda_A$  that approximates  $\tilde{\Lambda}$ , but that generally does not have the properties required of a density operator, such as a non-negative spectrum. The last step in MLFT is therefore to convert the ansatz state  $\Lambda_A$  into a “maximum likelihood” state  $\Lambda_{ML}$  by using an algorithm borrowed from MLST in Ref. [21]. We describe MLFT in more detail below.

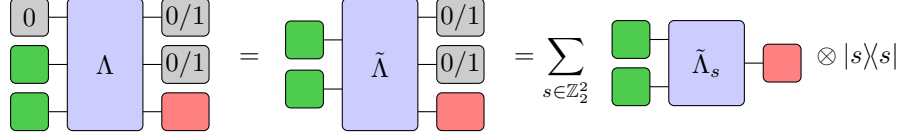


FIG. 2. Each circuit fragment can be identified with a density operator  $\Lambda$  on the joint Hilbert space of its input (left) and output (right) qubits. Classical inputs and outputs of a fragment (gray) correspond to qubits that are either prepared in the trivial state  $|0\rangle$  (labeled “0”) or measured in a fixed computational basis (labeled “0/1”), as appropriate. Quantum inputs (green, left) and outputs (red, right) correspond to qubits associated with cuts in a circuit. Due to the presence of trivial inputs, we only need to characterize a reduced state  $\tilde{\Lambda}$  on the Hilbert space of the quantum inputs and all outputs. Classical outputs, meanwhile, give the reduced state  $\tilde{\Lambda} = \sum_s \tilde{\Lambda}_s \otimes |s\rangle\langle s|$  a block-diagonal structure, where the block  $\tilde{\Lambda}_s$  is associated with the measurement of bitstring  $s$  on the classical outputs of the fragment.

MLFT (and MLST) begins by collecting measurement data to characterize the quantum state under consideration. In the case of the block-diagonal state  $\tilde{\Lambda}$ , one needs to essentially characterize expectation values

$$\langle \sigma_i \otimes \sigma_o \otimes z_c \rangle_{\tilde{\Lambda}} \equiv \text{tr} [\tilde{\Lambda} (\sigma_i \otimes \sigma_o \otimes z_c)] \quad (17)$$

for some complete basis of operators  $\{\sigma_i \otimes \sigma_o \otimes z_c\}$  on the target Hilbert space of  $\tilde{\Lambda}$ , where  $\sigma_i$ ,  $\sigma_o$ , and  $z_c$  are respectively operators on the quantum input, quantum output, and classical output of the fragment in question, with  $z_c$  strictly diagonal in the computational basis. MLST [21] collects data by performing informationally complete measurements of  $\tilde{\Lambda}$ , for example by choosing operators  $\sigma_{i,o}$  from the set of all Pauli strings  $\{\mathbb{1}, X, Y, Z\}^{\otimes Q_{i,o}}$ , and choosing  $z_c$  from the set of diagonal Pauli strings  $\{\mathbb{1}, Z\}^{\otimes C_o}$ . In the case of fragment tomography, however, we do not have direct access to the state  $\tilde{\Lambda}$ , and instead have access to the channel  $\mathcal{E}_{\tilde{\Lambda}}$ . It is therefore not possible to directly measure the degrees of freedom in  $\tilde{\Lambda}$  that are associated with inputs to the channel. Instead, MLFT characterizes the quantum input degrees of freedom in  $\tilde{\Lambda}$  by preparing an informationally complete set of states, making use of the fact that

$$\langle \rho_i^T \otimes \sigma_o \otimes z_c \rangle_{\tilde{\Lambda}} = \text{tr} [\mathcal{E}_{\tilde{\Lambda}} (\rho_i) (\sigma_o \otimes z_c)] \quad (18)$$

$$= \langle \sigma_o \otimes z_c \rangle_{\mathcal{E}_{\tilde{\Lambda}} (\rho_i)}, \quad (19)$$

where  $\rho_i^T$  denotes the transpose of  $\rho_i$ . Whereas the operators  $\sigma_o$  and  $z_c$  may still be chosen from the set of Pauli strings, the input state  $\rho_i$  is restricted to satisfy  $\text{tr} \rho_i = 1$ . This restriction excludes the possibility of choosing states  $\rho_i$  from an *orthogonal* basis for the space of the space of  $Q_i$ -qubit operators (such as the set of Pauli strings), but any *complete* basis will suffice. For example, one can choose input states from the basis of pure states  $\{|0\rangle, |1\rangle, |0\rangle + |1\rangle, |0\rangle + i|1\rangle\}^{\otimes Q_i}$ . For an unbiased basis, one can take tensor products of symmetric informationally complete (SIC) states of a single qubit, or even consider bases of multi-qubit SIC states. The practical advantages of using these bases, however, generally depend on the fidelity with which one can prepare

SIC states (similar considerations apply for the choice of measurement basis for quantum outputs [27]). Overall, for a given fragment one must prepare each of  $4^{Q_i}$  input states, and measure outputs in each of  $3^{Q_o}$  possible bases (for each quantum output qubit, the diagonal bases of  $X, Y, Z$ ), so fragment tomography requires  $O(4^{Q_i} 3^{Q_o})$  experiments.

After collecting an informationally complete set of data on the state  $\tilde{\Lambda}$ , a straightforward least-squares fitting procedure yields an empirical ansatz  $\Lambda_A$  for  $\tilde{\Lambda}$ , which is the MLFT analogue of the “experimentally noisy” matrix  $\mu$  described in the original MLST work [21]. The block diagonal structure of  $\tilde{\Lambda} = \sum_s \tilde{\Lambda}_s \otimes |s\rangle\langle s|$  implies that the least-squares fitting procedure can be performed independently for each block  $\tilde{\Lambda}_s$  of size  $2^{Q_i+Q_o} \times 2^{Q_i+Q_o}$ . Specifically,  $\tilde{\Lambda}_s$  is obtained by fitting to

$$\text{tr} [\tilde{\Lambda}_s (\sigma_i \otimes \sigma_o)] = p_s \langle \sigma_i \otimes \sigma_o \rangle_s, \quad (20)$$

where  $p_s$  is the probability of observing bitstring  $s$  on the classical output of a fragment, and  $\langle \sigma_i \otimes \sigma_o \rangle_s$  is the experimental expectation value of  $\sigma_i \otimes \sigma_o$  when observing bitstring  $s$ . Because it is constructed from a fit to noisy measurement data, the ansatz state  $\Lambda_A$  will generally have negative eigenvalues, which is not allowed for density operators. The final step in both MLST and MLFT is therefore to find the closest state to  $\Lambda_A$  that has no negative eigenvalues. To this end, MLFT borrows the “fast algorithm for subproblem 1” in Ref. [21], which essentially

- (i) diagonalizes  $\Lambda_A$ ,
- (ii) eliminates the most negative eigenvalue (setting it to zero),
- (iii) adds an equal amount to all other eigenvalues to enforce  $\text{tr} \Lambda_A = 1$ , and
- (iv) repeats steps (ii,iii) until there are no more negative eigenvalues.

As proven in Ref. [21], this algorithm finds the closest positive semidefinite state  $\Lambda_{\text{ML}}$  to  $\Lambda_A$  with respect to the metric induced by the 2-norm:  $\|A\|_2 \equiv \sqrt{\text{tr}(A^\dagger A)}$ . In

this sense,  $\Lambda_{\text{ML}}$  is the “most likely” state consistent with  $\Lambda_A$ . The only additional consideration for this algorithm when performing MLFT has to do with making use of block diagonal structure to diagonalize  $\Lambda_A$ : each block of size  $2^{Q_i+Q_o} \times 2^{Q_i+Q_o}$  can be diagonalized independently. The overall serial runtime of the algorithm to find  $\Lambda_{\text{LM}}$  from  $\Lambda_A$  is therefore  $O(2^{3(Q_i+Q_o)}N_c)$ , where  $N_c$  is the number of blocks in  $\Lambda_A$ , or equivalently the number of distinct bitstrings observed on the classical output of the fragment throughout tomography.

As an added bonus, the treatment of fragments and their dual states  $\Lambda$  as first-class objects in MLFT enables a straightforward tensor-network-based circuit reconstruction method, which in turn allows for the use of efficient numerical routines for circuit reconstruction. Rather than explicitly computing and summing over each term of the fragment recombination formula in Eq. (4), the basic idea is to think of the entire sum as a contraction of two tensors. We sketch out this idea in Figure 3, making use of the relationship between fragment states  $\Lambda$ , their reductions  $\tilde{\Lambda}$ , and diagonal blocks  $\tilde{\Lambda}_s$ . In total, the full probability distribution over measurement outcomes for a reconstructed circuit can be acquired by a tensor network contraction of reduced states  $\tilde{\Lambda}$ , and the individual probabilities of measuring any given bitstring at the output of a circuit can be acquired by a similar contraction of diagonal blocks  $\tilde{\Lambda}_s$ .

## V. NUMERICAL EXPERIMENTS

In order to test the benefits of MLFT in an application-agnostic setting, we run classical simulations of random unitary circuits (RUCs). Because the cost of circuit cutting scales exponentially with the number of cuts made to a circuit, we construct RUCs with a structure that makes them amenable to circuit cutting (see Figure 4). We then vary the number of qubits in a clustered RUC, as well as the number of clusters. For each choice of a number of qubits and a number of clusters, we fix a total budget of  $10^6$  queries to quantum hardware (known as “shots” or “trials” in e.g. Qiskit [22] or pyQuil [23]; the result of each query is a single bitstring representing one measurement outcome) and consider three methods to estimate the probability distribution over measurement outcomes at the end of a clustered RUC.

First, as a “standard” benchmark, we consider sampling an entire circuit  $10^6$  times without any circuit cutting or reconstruction, which we refer to as the method of *full* circuit execution. Second, we consider cutting a circuit into fragments, with each fragment corresponding to a cluster as shown in Figure 4, and reconstructing these fragments essentially as prescribed by the original circuit cutting work [16]. We refer to this second method as the *direct* method of circuit cutting and reconstruction<sup>b</sup>. A

fragment with  $Q_i$  quantum inputs and  $Q_o$  quantum outputs has  $4^{Q_i} \times 3^{Q_o}$  variants that must be simulated for circuit reconstruction, where each variant corresponds to a choice of state preparations and measurement bases on the quantum inputs and outputs of the fragment. We divide the budget of  $10^6$  queries evenly among all fragment variants, and simulate all variants accordingly to characterize and recombine fragments. Finally, we consider the full MLFT and recombination procedure outlined in Section IV, which we will refer to as the MLFT method. Note that the direct and MLFT methods only differ in the classical post-processing of fragment simulation results.

To compare the efficacy of these methods, we compute the fidelity of each estimated probability distribution over measurement outcomes,  $p_{\text{estimate}}$ , with the actual probability distribution  $p_{\text{actual}}$  that is determined by exact classical simulations of a circuit:

$$f = \left[ \sum_s \sqrt{p_{\text{actual}}(s) p_{\text{estimate}}(s)} \right]^2, \quad (21)$$

where  $p_{\text{actual}}(s), p_{\text{estimate}}(s)$  are, respectively, the probabilities of measuring the  $N$ -qubit state (bitstring)  $s \in \mathbb{Z}_2^N$  according to the distributions  $p_{\text{actual}}, p_{\text{estimate}}$ . The fidelity defined in Eq. (21) is an analogue of the quantum state overlap  $|\langle \phi | \psi \rangle|^2$  for classical probability distributions. The only caveat in our calculation of fidelities is that they are only well defined when dealing with valid (non-negative and normalized) probability distributions, whereas the direct circuit cutting method generally yields an unnormalized distribution that may have negative entries. We therefore convert the distribution yielded by the direct method into a valid probability distribution by eliminating all negative entries (setting them to zero), and normalizing the distribution.

Figure 5 shows the infidelities,  $1 - f$ , of the probability distributions yielded by each simulation method. To ensure that results are not sensitive to the specific choice of random gates, these infidelities are averaged over 100 instances of each clustered RUC. Figure 5 also shows the standard deviation  $\sigma_f$  in the fidelity  $f$  over each set of 100 instances;  $\sigma_f$  quantifies the robustness of each method with respect to circuit variations (for a fixed circuit structure).

The key takeaway from Figure 5 is that the MLFT method introduced in this work always outperforms the direct method from past work. MLFT infidelities are always lower than direct infidelities, and are more robust to circuit variations. This result is consistent with theoretical arguments that MLFT finds the “most likely”

<sup>b</sup> To minimize classical computing costs, our actual implementa-

tion of the “direct” method involves performing the fragment tomography and recombination procedures discussed in Section IV, but skipping the “maximum likelihood” corrections to fragment models. This procedure is mathematically equivalent (which is to say that it yields an identical output) to that in Ref. [16].

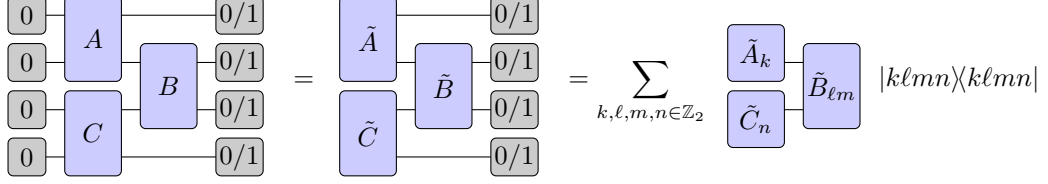


FIG. 3. Fragment recombination of three circuit fragments  $A, B, C$  as a tensor network contraction problem. The full probability distribution over measurement outcomes for a reconstructed circuit can be represented by a tensor contraction of the reduced states  $\tilde{A}, \tilde{B}, \tilde{C}$ , obtained by performing MLFT on the fragments. Meanwhile, the probability to measure a given bitstring  $k\ell mn$  (i.e. a concatenation of  $k, \ell, m, n \in \mathbb{Z}_2$ ) on the output of the fragment is given by the contraction of the diagonal blocks  $\tilde{A}_k, \tilde{B}_{\ell m}, \tilde{C}_n$ . Note that the lack of classical inputs to fragment  $B$  implies that  $\tilde{B} = B$ .

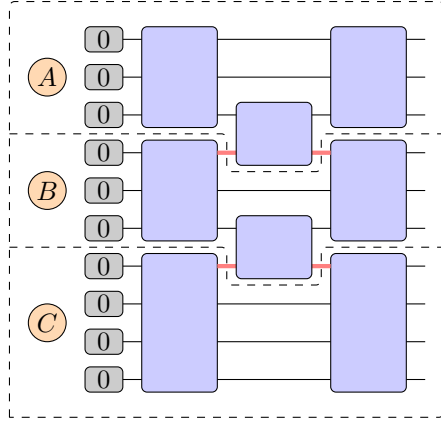


FIG. 4. Random unitary circuit (RUC) of ten qubits split into three clusters. Qubits are first split among clusters as evenly as possible, and each cluster is prepared in a random state by the application of a Haar-random unitary gate [28, 29]. Adjacent clusters are then entangled with random two-qubit gates, before again applying a layer of random unitaries on all clusters. A clustered RUC is cut into fragments (labeled  $A, B, C$ ) by cutting the bottom legs (shown in red) of every inter-cluster entangling gate.

fragment model consistent with noisy measurement data. Although we only consider shot noise in this work, it would be interesting to see how the benefits of MLFT change with the introduction of additional noise such as measurement and gate errors. We defer a study of the effect of such errors to future work.

Both the direct and MLFT methods perform worse than full circuit execution for small circuits. However, their fidelities scale more favorably with circuit size, and they eventually outperform the method of full circuit execution. This result is surprising at first glance, in light of the fact that the circuit cutting methods use strictly fewer quantum computing resources: their  $10^6$  query budget is spent on executing smaller circuits (namely, fragment variants). The better performance of the circuit cutting methods can be explained by the fact that they use their query budget in a targeted manner that exploits circuit structure, rather than blindly sampling the entire circuit. However, when circuits are sufficiently small for

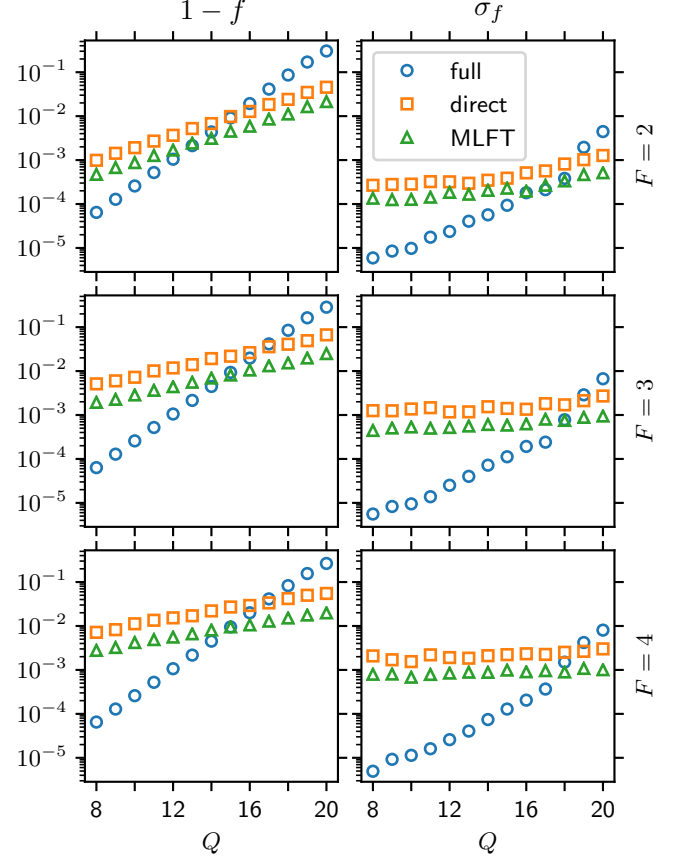


FIG. 5. Average infidelity ( $1 - f$ , left column) and the standard deviation of the fidelity ( $\sigma_f$ , right column) in simulations of clustered random unitary circuits (RUCs) with  $Q$  qubits and  $F = 2, 3, 4$  clusters (top, middle, and bottom rows, respectively). The number of clusters determines the corresponding circuit structure according to Figure 4. Different markers correspond to simulations of the full circuit ("full"), or simulations via cutting and recombination before and after maximum likelihood corrections ("direct" and "MLFT"). Each point is computed by simulating 100 instances of a clustered RUC, with a budget of  $10^6$  quantum hardware queries ("shots" or "trials") for each RUC.

the number of queries ( $10^6$ ) to explore the sample space of the entire circuit ( $2^Q$ , for a  $Q$ -quit circuit), full circuit sampling performs better than circuit cutting because it does not waste resources on characterizing fragments’ “virtual” degrees of freedom, associated with quantum inputs and outputs.

We can also understand the better scaling of the circuit cutting methods by considering the difficulty of estimating a probability distribution defined by a  $Q$ -qubit RUC by (i) sampling the full circuit directly, versus (ii) sampling all fragment variants for circuit reconstruction. The first task requires, in principle, exploring a sample space of size  $2^Q$ . If a circuit is cut into  $F$  fragments with  $K$  cuts, then each fragment will consist of  $\sim Q/F$  qubits and have  $\sim K/F$  quantum inputs and outputs, for a total of  $\sim 4^{K/F} \times 3^{K/F}$  fragment variants. Altogether, circuit cutting requires exploring a sample space of size  $\sim 2^{Q/F}$  for  $\sim F \times 4^{K/F} \times 3^{K/F}$  fragment variants. If the number of cuts ( $K$ ) is independent of the number of qubits ( $Q$ ), as is the case with our clustered RUCs, then circuit cutting reduces the overall sample space volume from  $2^Q$  to  $O(2^{Q/F})$ . This argument is loosely mirrored by the observation that the infidelity  $1 - f$  as a function of qubit number  $Q$  in Figure 5 has a slope  $\partial \log(1 - f) / \partial Q \approx 0.3/F$  (where we treat the “full” method as having only one “fragment”). The linear growth of log-infidelity must eventually end, as  $\log(1 - f)$  is bounded above by 1, but away from this bound a slope  $\partial \log(1 - f) / \partial Q \propto 1/F$  is consistent with a problem difficulty that scales exponentially in  $Q/F$ .

## VI. CONCLUSIONS AND OUTLOOK

Circuit cutting is a promising technique for reducing the qubit requirements of running clustered quantum circuits. We have introduced improved circuit cutting methods by minimizing associated classical computing costs (with an exponential improvement over previous methods), and by using MLFT to reconstruct the “most likely” probability distribution defined by a quantum circuit, given the measurement data obtained from its fragments. To test our ideas in an application-agnostic setting, we ran classical simulations of random unitary circuits, which demonstrate the advantages of MLFT compared to the original circuit cutting method. Moreover, we provide both numerical evidence and theoretical arguments for the advantages of circuit cutting as a standard technique for running clustered circuits on quantum

hardware, even when full circuit execution is possible.

Our work opens several avenues for the improvement and application of circuit cutting techniques. For example, MLFT guarantees that fragment models satisfy appropriate self-consistency conditions, but MLFT makes no use of the fact that each fragment corresponds to a *unitary* quantum channel. Furthermore, our present work neglects the effects of hardware errors that are important to consider in the context of NISQ devices. Because MLFT has the capability to mitigate shot noise, we expect the advantages of MLFT over full circuit execution to be enhanced when additionally considering the effects of hardware errors. We likewise expect unitarity constraints to provide additional benefits for mitigating sources of noise. Our work thus complements ongoing efforts that study the benefits of circuit cutting in the presence of hardware errors, which have generally found that circuit cutting helps mitigate the effects of noise [30]. Having framed fragment characterization as a tomography task, it would also be interesting to adapt and apply different quantum process tomography techniques [31] to the task of circuit cutting, and compare their performance and cost to that of MLFT.

As a final point, we note that circuit cutting in its current form estimates a probability distribution associated with a given circuit. Ideally, one would like to *sample* this probability distribution, avoiding the need to reconstruct a distribution that is ultimately defined over an exponentially large space of possible measurement outcomes. To this end, our work makes important progress in understanding the mechanics of circuit cutting, by providing a convenient and efficient framework for thinking about individual circuit fragments. We hope that this framework will help in achieving the ultimate goal of sampling a quantum circuit by sampling its fragments.

## ACKNOWLEDGMENTS

We acknowledge helpful discussions with Yuri Alexeev, Bradley Pearlman, Teague J. Tomesh, and Wei Tang. This material is based upon work supported by Laboratory Directed Research and Development (LDRD) funding from Argonne National Laboratory, provided by the Director, Office of Science, of the U.S. Department of Energy under contract DE-AC02-06CH11357. This research also used the resources of the Argonne Leadership Computing Facility, which is DOE Office of Science User Facility supported under Contract DE-AC02-06CH11357.

- 
- [1] J. Preskill, *Quantum* **2**, 79 (2018).
- [2] G. Wendin, *Reports on Progress in Physics* **80**, 106001 (2017).
- [3] M. Kjaergaard, M. E. Schwartz, J. Braumüller, P. Krantz, J. I.-J. Wang, S. Gustavsson, and W. D. Oliver, *Annual Review of Condensed Matter Physics* **11**, 369 (2020).
- [4] F. Arute, K. Arya, R. Babbush, D. Bacon, J. C. Bardin, R. Barends, R. Biswas, S. Boixo, F. G. S. L. Brandao, D. A. Buell, *et al.*, *Nature* **574**, 505 (2019).
- [5] S. Boixo, S. V. Isakov, V. N. Smelyanskiy, R. Babbush, N. Ding, Z. Jiang, M. J. Bremner, J. M. Martinis, and

- H. Neven, *Nature Physics* **14**, 595 (2018).
- [6] S. Lloyd, *Science* **273**, 1073 (1996).
- [7] I. M. Georgescu, S. Ashhab, and F. Nori, *Reviews of Modern Physics* **86**, 153 (2014).
- [8] E. Farhi, J. Goldstone, and S. Gutmann, [arXiv:1411.4028 \[quant-ph\]](https://arxiv.org/abs/1411.4028) (2014).
- [9] S. Hadfield, Z. Wang, B. O’Gorman, E. G. Rieffel, D. Venturelli, and R. Biswas, *Algorithms* **12**, 34 (2019).
- [10] N. Moll, P. Barkoutsos, L. S. Bishop, J. M. Chow, A. Cross, D. J. Egger, S. Filipp, A. Fuhrer, J. M. Gambetta, M. Ganzhorn, *et al.*, *Quantum Science and Technology* **3**, 030503 (2018).
- [11] V. Dunjko, J. M. Taylor, and H. J. Briegel, *Physical Review Letters* **117**, 130501 (2016).
- [12] J. Biamonte, P. Wittek, N. Pancotti, P. Rebentrost, N. Wiebe, and S. Lloyd, *Nature* **549**, 195 (2017).
- [13] S. Endo, S. C. Benjamin, and Y. Li, *Physical Review X* **8**, 031027 (2018).
- [14] A. Kandala, K. Temme, A. D. Córcoles, A. Mezzacapo, J. M. Chow, and J. M. Gambetta, *Nature* **567**, 491 (2019).
- [15] S. Bravyi, G. Smith, and J. A. Smolin, *Physical Review X* **6**, 021043 (2016).
- [16] T. Peng, A. Harrow, M. Ozols, and X. Wu, [arXiv:1904.00102 \[quant-ph\]](https://arxiv.org/abs/1904.00102) (2019).
- [17] W. Li, S. Li, and Y. Jiang, *The Journal of Physical Chemistry A* **111**, 2193 (2007).
- [18] H. Li, W. Li, S. Li, and J. Ma, *The Journal of Physical Chemistry B* **112**, 7061 (2008).
- [19] M. S. Gordon, D. G. Fedorov, S. R. Pruitt, and L. V. Slipchenko, *Chemical Reviews* **112**, 632 (2012).
- [20] A. Peruzzo, J. McClean, P. Shadbolt, M.-H. Yung, X.-Q. Zhou, P. J. Love, A. Aspuru-Guzik, and J. L. O’Brien, *Nature Communications* **5**, 4213 (2014).
- [21] J. A. Smolin, J. M. Gambetta, and G. Smith, *Physical Review Letters* **108**, 070502 (2012).
- [22] H. Abraham, A. Offei, I. Y. Akhalwaya, G. Aleksandrowicz, T. Alexander, G. Alexandrowics, E. Arbel, A. Asfaw, C. Azaustre, A. Ngoueya, *et al.*, “Qiskit: An open-source framework for quantum computing,” (2019).
- [23] R. S. Smith, M. J. Curtis, and W. J. Zeng, “A practical quantum instruction set architecture,” (2016), [arXiv:1608.03355 \[quant-ph\]](https://arxiv.org/abs/1608.03355).
- [24] A. Jamiołkowski, *Reports on Mathematical Physics* **3**, 275 (1972).
- [25] M.-D. Choi, *Linear Algebra and its Applications* **10**, 285 (1975).
- [26] M. Jiang, S. Luo, and S. Fu, *Physical Review A* **87**, 022310 (2013).
- [27] R. B. A. Adamson and A. M. Steinberg, *Physical Review Letters* **105**, 030406 (2010).
- [28] K. Zyczkowski and M. Kus, *Journal of Physics A: Mathematical and General* **27**, 4235 (1994).
- [29] J. Emerson, E. Livine, and S. Lloyd, *Physical Review A* **72**, 060302 (2005).
- [30] T. Ayral, F.-M. L. Régent, Z. Saleem, Y. Alexeev, and M. Suchara, [arXiv:2005.12874 \[quant-ph\]](https://arxiv.org/abs/2005.12874) (2020), accepted in ISVLSI 2020.
- [31] G. Torlai, C. J. Wood, A. Acharya, G. Carleo, J. Carrasquilla, and L. Aolita, [arXiv:2006.02424 \[quant-ph\]](https://arxiv.org/abs/2006.02424) (2020).